Effect of cushion types on the seismic response of structure with disconnected pile raft foundation

Yang Yang[1, 2]; Yi Pik Cheng[2]; Weiming Gong[1]; Hong Fan[3]; Guoliang Dai[1]

[1] Key Laboratory of Concrete and Prestressed Concrete Structures of Ministry of Education, Southeast University, Nanjing, 211189, China
[2] Department of Civil, Environmental and Geomatic Engineering, University College London, UK
[3] State Key Laboratory of Nuclear Power Safety Monitoring Technology and Equipment, China Nuclear Power Engineering Co., Ltd., Shenzhen 518029, China

Corresponding Author: Weiming Gong, Professor, Key Laboratory of Concrete and Prestressed Concrete Structures of Ministry of Education, Southeast University, Nanjing, 211189, China. E-mail: wmgong@seu.edu.cn

Abstract: In recent years, the benefits of reducing the impacts of the earthquake on the seismic response of disconnected pile raft foundation (DPRF) have simulated increasing research on this type of foundations to provide references for foundation design. One effective way to study the seismic response of soil-structures is to investigate the scaled models in 1-g shaking table tests. In this paper, a series of scaled 1-g shaking table tests were carried out to study the seismic response of scaled nuclear power stations with DPRF under earthquake excitations founded in clay. Three different cushion types were adopted to study their different effects on the seismic response of the structure and the foundation. The fundamental structural frequency, horizontal displacement, and acceleration results showed that cushion A with well-graded gravel and cushion B with a mixture of two gravel sizes were better than cushion C with a single gravel size. Although cushion type had an insignificant influence on bending moments of the disconnected piles, the maximum bending moments in all cases were found to be proportional to the near-pile acceleration. Furthermore, design engineers should pay more attention to the rocking of a structure with DPRF under earthquake loads.

Keywords: shaking table tests; gravel cushion; disconnected pile raft foundation; seismic response; dynamic bending moment

1 Introduction

Connected pile raft foundation (CPRF) has been successfully used in many projects and has been described by many authors for it has adequate bearing-capacity, and it can also control the settlements on a deep deposit of clay [1-6]. However, under earthquake excitation, high horizontal shear stresses and bending moments are generated in the connected area between pile and raft. Recently DPRF has been adopted in several projects [7-8]. The DPRF reduces shear stresses and bending moments of pile head and the seismic response of the structure, but the horizontal displacement of the structure under earthquake is greater than CPRF [9]. For better understanding the characteristic of DPRF, more research into the seismic response of the DPRF is needed.

Many studies about DPRF have been carried out recently. DPRF consists of three elements: pile, gravel cushion and raft [10]. In contrast to the conventional CPRF, there is a layer of gravel cushion between the piles and the raft, transmitting loads from the raft to the piles and the soil. The performance of DPRF in static load conditions has been evaluated in both numerical and experimental studies. Liang *et al*. and Ata *et al*. found that cushion can adjust the load-sharing ratios such that the load is transferred more evenly among piles, and the thickness of the cushion has considerable effects on adjusting the load-sharing ratio of piles and soil [11-12]. El Sawwaf compared the influence of connected and disconnected short piles on the raft characteristic under eccentrical vertical load, which turned out that the CPRF had a more remarkable improvement in the raft behaviour [13]. Parametric studies, including piles number, diameter, length, and raft thickness, have been carried out by Tradigo *et al*. [14-15], and the study showed that DPRF provided an economical alternative for a CPRF. El Kamash *et al*. investigated three cushion types, including sand, sandy gravel and EPS Geofoam, and the results turned out it had an insignificant effect on the settlements of the DPRF [16]. The DPRF in static load conditions is an efficient system based on the previous studies; however, the behaviour of DPRF in dynamic load conditions should be studied urgently for safety requirement. In reality, earthquake shaking occurs in two orthogonal directions simultaneously. The simultaneous action of the two orthogonal horizontal ground motions has proven to have a significant impact on the inelastic demand of structures. Ignoring this interaction may result in a significant underestimation of ductility in pile design

[17]. ASCE and Eurocode suggest combining the 100% and 30% of response obtained from the two directions due to this bidirectional interaction [18-19]. Unfortunately, a very few research on DPRF to date has been performed without considering this interaction, and it is not considered in this paper. The seismic response studies of DPRF under earthquake excitations have been increasing in recent years. Xu and Fatahi studied the seismic performance of a mid-rise building with geosynthetic-reinforced cushioned end-bearing piles using FLAC3D software, and found that the base shear forces of the superstructure, shear forces and bending moments of piles were decreased compared with CPRF [20]. Azizkandi *et al*. demonstrated that CPRF had much higher lateral stiffness and could reduce the lateral movements of the structure more effectively than DPRF, using 1-g shaking table tests and finite element analyses [21]. Baziar *et al*. and Ko *et al.* showed that both the edge pile bending moment and the amplitude of horizontal acceleration for the DPRF are smaller than those of the CPRF [22-23]. Saadatinezhad *et al.* found that DPRF led to significantly less shear force and bending moments along the piles [24]. Based on the centrifuge test, Ha *et al*. found that using a larger stiffness cushion layer, the foundation had less vertical settlement than that of the shallow foundation without pile [25]. Dhanya *et al*. invested the seismic response of a two-stories building with raft foundation resting on sand-rubber mixture using Finite Element Method, and the seismic settlement and lateral deformation of the structure were reduced, because of the energy-absorbing benefit characteristics of the sand-rubber mixture [26]. In general, the dynamic studies focused on the comparison of DPRF and CPRF, the characteristic of reducing the structural seismic response of DPRF, effects of pile parameters and cushion thickness of DPRF on the seismic response. Nevertheless, the investigation on the effect of gravel cushion type on the seismic response of DPRF under earthquake excitation in clay soil is not available.

In this study, a series of 1-g shaking table tests were conducted to gain insights into the seismic response of a scaled nuclear power station with DPRF in clay. Most nuclear power stations are rest on rock areas; however, with the site limitations, construction technology development and other considerations, nuclear power stations rested in clay are worth studying. Three types of cushions were adopted to study the effects of cushion type on the seismic response of the scaled model. Each cushion case consisted of one 0.05 g white noise excitation and three earthquake excitations with different intensities. The acceleration recorded data under the white noise excitation were utilised to generate model parameters, including damping ratio and fundamental frequency, of the scaled model via random decrement technique (RDT) and the wavelet transform (WT) methods. The soil nonlinearity, the isolation effect of each cushion, the displacement characteristics, and the bending moment results were analysed. In addition, the acceleration response of near-pile and far-field soil was investigated to better understand the effect of soil-pile interaction on the seismic response.

2 Shaking table test program

2.1 Model configuration

All results and dimensions in this paper are the original shaking table test recorded results and small-scale model dimensions under 1 g condition. The shaking table tests were conducted at the Key Laboratory of Concrete and Prestressed Concrete Structures of Ministry of Education, Southeast University, China. The uniaxial shaking table is 4 m × 6 m. It can output a maximum horizontal acceleration of 0.3g without loading and 1.5 g under the maximum allowable load of 25 tons. The maximum displacement tolerance of the shaking table is ±250 mm, and the maximum velocity is 600 mm/s. The working frequency ranges from 0.1 Hz to 50 Hz.

A laminar shear model box of 2 m (length), 2.0 m (width), and 1.3 m (height) was used, and it allows the soil to deform under uniaxial excitations. The inside surface of the laminar shear model box was covered by a thick 10 cm sponge and a rubber membrane to absorb the excitation energy on the boundary to avoid wave interference. After the laminar shear model box was filled with soil, a series of shaking table tests were carried out on the free-field soil. The boundary effect of the laminar shear model box on the dynamic characteristic of the soil has been found to be neglectable by the results of two different accelerometers near and far from the boundary of the laminar shear model box. The difference in the peak soil surface acceleration between those two accelerometers is about 5%. The fundamental frequencies and damping ratios are almost the same.

It is known that the shaking table test is difficult in providing the soil stress as the prototype; however, the model was designed based on the scaled (one-tenth) Chinese III generation nuclear power station. And it was the same model as the previous study about CPRF [27]. The scaled structure model contains a cylinder, dome and cuboid, with a scaling factor of 1/25. The height, diameter, and thickness of the cylinder are 243 mm, 216 mm, and 4 mm, respectively, and it was made of aluminium. The height of the dome and thickness were 45 mm and 50 mm, and it was made of iron. The photograph of the structure will be shown in the following section. The cuboid was made of polymethyl methacrylate with a density of 1.18 g/cm^{3}, and the length, width, height and thickness of the cuboid were 442 mm, 328 mm, 148 mm and 2 mm. The inside of the structure was fully filled with iron plates to provide additional loads. The length, width and thickness of the raft were 476 mm, 362 mm and 32 mm, and it was made of aluminium. The foundation of the model consists of 12 aluminium tube piles, the same as the material was employed in a series of centrifuge tests, and the diameter and thickness of the tube pile are 28 mm and 1 mm, respectively.

The Nanjing clay sampling site is located at southeast of the Nanjing City of Jiangsu Province, and more information about the clay could be found in Zeng *et al.* [28]. The clay collected from the sampling site was placed to the laminar shear model box layer by layer. Each time the crane poured about 0.4 m^3 clay into the box, and then the soil was flattened. Note that the surface of every layer was roughened to build an integrated soil. The fundamental period of the soil is about 0.1 s, and the calculated shear wave velocity of the soil is 48 m/s. The soil properties of the tested clay are listed in Table 1. The particle size distribution of clay was shown in Figure 1(a). The triaxial test samples were collected from the laminar shear model box after the shaking table tests. The cohesion 7.2 kPa and internal friction angle 21° were obtained from consolidated drained triaxial tests performed in the Nanjing Forestry University, using the GDS triaxial apparatus. The diameter and the height of the soil sample are 70 mm and 125 mm, respectively. The loading rate of the strain-controlled consolidated drained triaxial test was 0.006 mm/min. In addition, three cases with the confining pressure 100 kPa, 200 kPa, and 300 kPa, were conducted in the test.

Table 1 Soil properties.

Soil properties	Value	Soil properties	Value
Density (kg/m^3)	1780	Liquid limit, w_P (%)	28.8
Water content, w(%)	23.52	Cohesion, c(kPa)	7.2
Liquid limit, w_L(%)	46.6	Internal friction angle, φ (°)	21

2.2 Cushion material properties

Three types of cushion were designed to investigate the effect of cushion types on the seismic response of the nuclear power station with the DPRF. The overall range of particle sizes of the cushions was based on a previous project [29]. The thickness of the cushion was 50mm, which is about two times of the pile diameter. The first cushion type was a well-graded gravel cushion, named cushion A. Figure 1 illustrates the particle grading curve of cushion A with D_{50} of 3.5 mm and a size range of 2 mm to 10 mm. The second cushion consisted of mixtures of two types of gravels in a ratio of 3:1, the major proportion was smaller particle diameters ranging from 2 mm to 5 mm, and the minor proportion was larger particle diameters ranging from 5 mm to 10 mm; this cushion is named cushion B. The last cushion consists of gravel particles of the smaller size range only, with particle diameter ranging from 2 mm to 5mm. The cushions were prepared at their maximum dry densities, which are 1.682×10^3 kg/m^3, 1.633×10^3 kg/m^3, and 1.581×10^3 kg/m^3 for cushion A, cushion B, and cushion C, respectively. The normalised dynamic shear modulus and damping ratios were obtained from a series of resonant column tests in the Nanjing Forestry University using the Stokoe resonant column apparatus. The test results of each gravel cushion at the confining pressure of 20 kPa are shown in Figure 2.

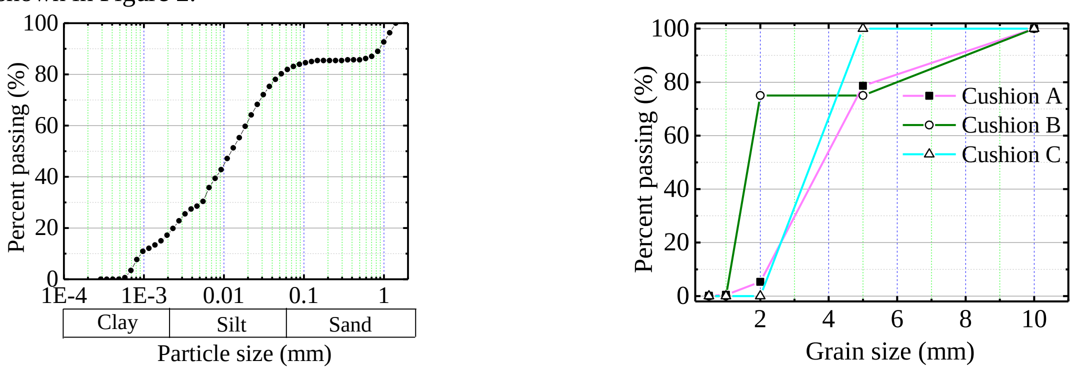

(a) (b)

Figure 1 Particle size distribution: (a) Clay; (b) cushions.

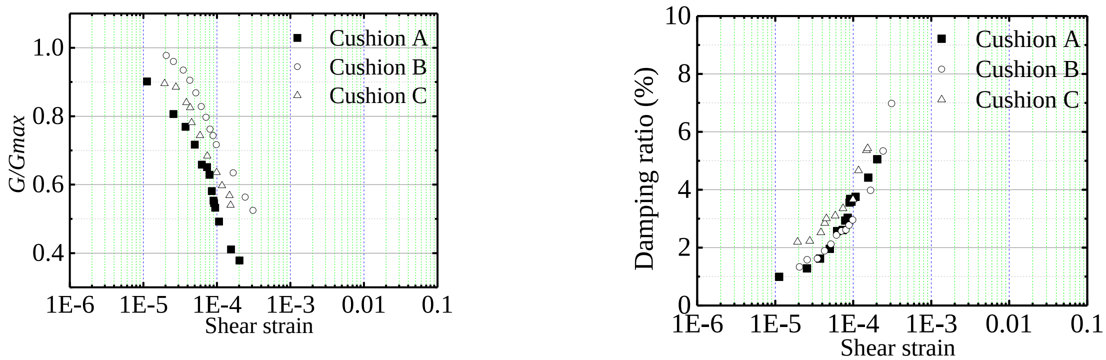

(a) (b)

Figure 2 Resonant column test results under confining pressure of 20 kPa: (a) normalised dynamic shear modulus; (b)damping ratios.

2.3 Test setup

The soil and nuclear power station scaled model in the laminar shear model box was instrumented with various sensors, including strain gauges on four piles, accelerometers A1 to A2 on the structure, accelerometer A3 on the raft, accelerometers A4 to A10 in the soils, laser displacement meters LS1 to LS3 on the structure and LS4 on the laminar shear model box, as illustrated in Figure 3. The resistance value of strain gauges used in the model is 120.3±0.1 and the sensitivity is 2.23±1%. The accelerometers horizontal sensitivity is less than 5% and mounted resonant frequency is 40,000 Hz. Four piles, named P1 to P4, were instrumented with strain gauges to identify the bending moment along the piles during excitation. P1 and P3 were located at the first row, and P4 and P2 were located at the second row. Six pairs of strain gauges were mounted along the opposite surfaces of each instrumented pile. The first level of strain gauges was 50 mm depth below the soil surface, and the distance between every two measured points was 100 mm. Three accelerometers labelled A1 to A3 were mounted on the structure top, structure middle, and raft, respectively. Two accelerometers labelled A4 and A5 were used to record the accelerations of the soil among piles. Four accelerometers labelled A6 to A9 were used to measure the accelerations of the soil far from piles. The vertical distance between any two accelerometers in the soil was 300 mm. Accordingly, A4 and A5 measured the near-pile accelerations, and A6 to A9 measured the far-field accelerations. An additional accelerometer A10 was embedded in the gravel cushion between the soil surface and the raft. Two laser displacement meters, labelled LS1 and LS2, were designed to record the vertical displacement of the structure, and the other two laser displacement meters, LS3 and LS4, were equipped on the shelf to monitor the horizontal displacement with respect to the ground.

2.4 Applied ground motion and test program

Four series of shaking table tests were conducted to investigate the seismic response of the nuclear power station with a DPRF. The detailed test programs are summarised in Table 2. Three different cushions, including cushion A, cushion B, and cushion C, were utilised in the shaking table tests; they were named case A, case B, and case C, respectively.

For each series of tests, the soil and the nuclear power station scaled model was excited by white noise and three earthquake ground motions (including one artificial ground motion and two natural ground motions). Figure 4 shows the time history acceleration and response spectrum of each applied ground motion in the tests. The artificial ground motion, named YG, was generated based on the EUR soft design response spectrum, and two ground motions consisted of the 1985 Mexico City earthquake wave (MEX) and 1940 El Centro earthquake wave (EL) [9]. The MEX and EL represent long-period ground motion and short-period ground motion, respectively, based on the dominant frequency; that is why those two ground motions were adopted in the tests. Figures 4(c) and (d) illustrate the scaled ground motions. The test ID is labelled to indicate the cushion type, the input excitation, and the excitation amplitude. The first character in the label is A, B, or C, indicating cushion A, cushion B, and cushion C. The second character in the label is W, Y, M, or E, indicating the white noise, the YG, the MEX, and the EL ground motion, respectively. The last number indicates the excitation amplitude with the design acceleration of 0.1, 0.2 and 0.3 g, corresponding to the designed modelled acceleration of 0.3, 0.6 and 0.9 g, respectively. For example, the test ID AY1 represents the model with cushion A, excited by the YG ground motion with the designed model acceleration amplitude of 0.3 g. The acceleration scaling factor (S_a) in shaking table tests is typically around 1-3 [30]; in this case, S_a is taken as 3 based on the performance of the shaking table apparatus. The detailed dimensional analyses of the geometry, material and dynamic properties are shown in Table 3 [27]. The peak recorded input acceleration (measured by A9) was different from the designed model acceleration due to the excitatory limitation of the shaking table; for instance, the designed model peak acceleration for AY1 was 0.3 g; however, the recorded input acceleration by A9 was 0.212 g due to the limitation in the calibration process. All the recorded input accelerations by A9 are illustrated in Table 2.

Table 2 Test programs.

Cushion	Test ID	Ground motion	Designed acc. (g)	Designed model acc. (g)	Recorded input acc. (g)
	AW0	white noise	0.05	0.05	-
	AY1	YG	0.10	0.30	0.212
	AE1	EL	0.10	0.30	0.258
	AM1	MEX	0.10	0.30	0.294
A	AY2	YG	0.20	0.60	0.371
	AE2	EL	0.20	0.60	0.572
	AM2	MEX	0.20	0.60	0.587
	AY3	YG	0.30	0.90	0.563
	AE3	EL	0.30	0.90	0.542
	AM3	MEX	0.30	0.90	0.951
	BW0	white noise	0.05	0.05	-
	BY1	YG	0.10	0.30	0.192
	BE1	EL	0.10	0.30	0.239
	BM1	MEX	0.10	0.30	0.291
B	BY2	YG	0.20	0.60	0.373
	BE2	EL	0.20	0.60	0.546
	BM2	MEX	0.20	0.60	0.594
	BY3	YG	0.30	0.90	0.545
	BE3	EL	0.30	0.90	0.515
	CW0	white noise	0.05	0.05	-
	CY1	YG	0.10	0.30	0.205
	CE1	EL	0.10	0.30	0.228
	CM1	MEX	0.10	0.30	0.314
C	CY2	YG	0.20	0.60	0.372
	CE2	EL	0.20	0.60	0.493
	CM2	MEX	0.20	0.60	0.608
	CY3	YG	0.30	0.90	0.526
	CE3	EL	0.30	0.90	0.546

Table 3 Scaling factor in the shaking table tests.

	Quantity	Symbol	Formula	Scaling factors (Model / Prototype)
Geometry property	Length, l	S_l	S_l	1/25
	Area, A	S_A	S_l^2	0.0016

Material property	Moment of inertia, I	S_I	S_l^4	0.00000256
	Modulus of elasticity, E	S_E	S_E	1
	Strain, ε	S_ε	/	1
	Poisson's ratio, μ	S_μ	/	1
	Density, ρ	S_ρ	$S_E/(S_a \cdot S_l)$	12.5
	Acceleration of gravity, g	S_g	1	1
Dynamic property	Mass, M	S_M	$S_E S_l^2/S_a$	5.33E-4
	Acceleration, a	S_a	S_a	3
	Velocity, v	S_v	$(S_l \cdot S_a)^{0.5}$	0.3464
	Period, T	S_T	$S_l^{0.5} \cdot S_a^{-0.5}$	0.1155
	Frequency, f	S_f	$S_l^{-0.5} \cdot S_a^{0.5}$	8.6603
	Damping, c	S_c	$S_E \cdot S_l^{1.5} \cdot S_a^{-0.5}$	0.0046

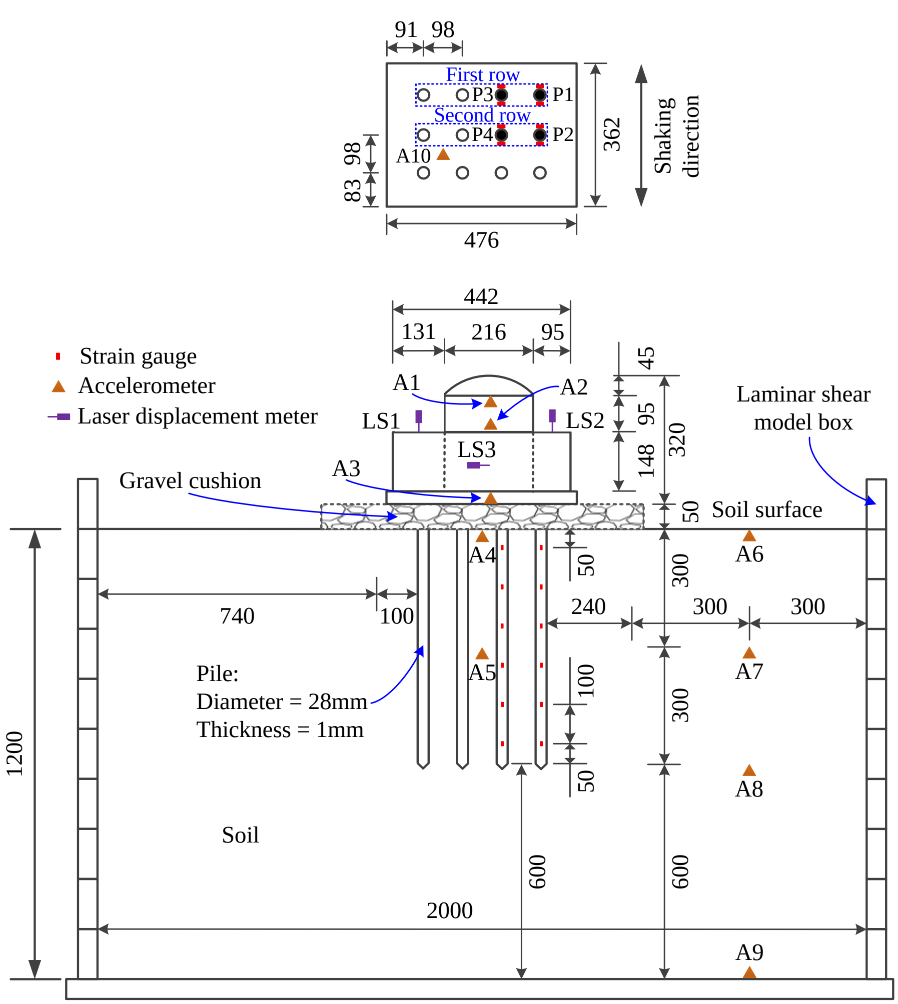

(a)

(b)

Figure 3 Scaled model and sensor locations: (a) The schematic diagram of the test; (b) photograph of the test.

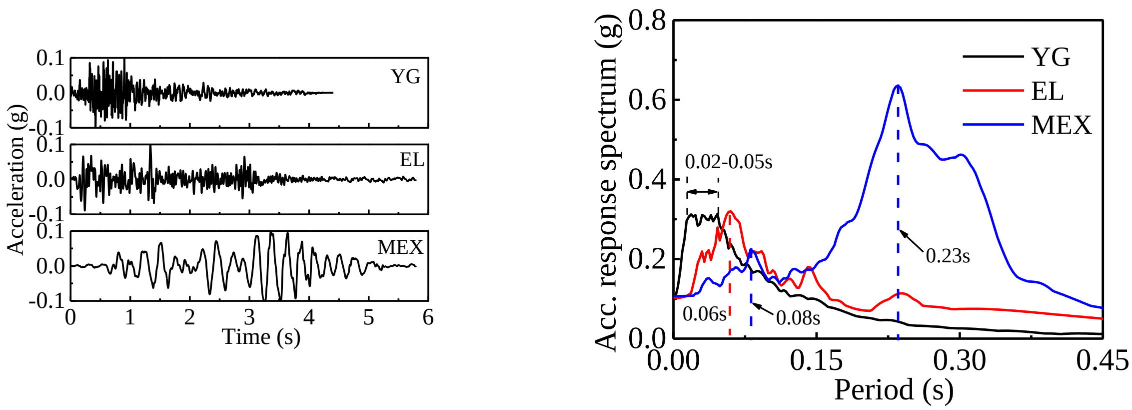

(a) (b)

Figure 4 Applied ground motions: (a) time history acceleration; (b) response spectrum.

3 Acceleration results and discussion

3.1 System frequency

The structural, raft and soil response produced by the white noise were selected to identify the model parameters of the scaled model. Using the white noise excitation cases AW0, BW0, and CW0, the measured acceleration data at various locations of the model were carefully analysed in order to obtain the natural frequency and damping ratio of each cushioned system. First, the singular spectrum analysis (SSA) was used to remove the noise from the measured acceleration (measured at measurement points A1, A2, A3, and A4). Based on the singular value decomposition (SVD), SSA can decompose a signal into several independent components, including the trend, periodic, and noise. Thus, the SSA can effectively realise the decomposition and reconstruction of signals, which is always used to remove the noise of the original data [31]. More detailed information regarding the SSA is available in Ma *et al.* [32] and Niu *et al.* [33]. Herein, 95% of the measured data at each location (structure-top, structure-middle, raft, and soil surface) is used to reconstruct the signal, aiming to remove the noise of the recorded data. Second, the random decrement technique (RDT) and the wavelet transform (WT) methods were applied to estimate the natural frequency and damping ratio based on the processed data from the last step. The RDT is an effective method to convert the random structural response induced by white noises to a free vibration response [34]. Moreover, the free vibration response can be decoupled into N relevant modes of the structure:

$$x(t) = \sum_{j=1}^{N} A_j e^{-\zeta_j \omega_{nj} t} \sin\left(\sqrt{1-\zeta_j^2}\,\omega_{nj} t + \varphi_j\right) \tag{1}$$

where A_j is the magnitude, ζ_j is the damping ratio, ω_{nj} is the natural angular frequency, and φ_j is the phase associated with the j_{th} mode. The WT is a linear transformation, which decomposes a signal via basis functions that are simply dilations and translations of the parent wavelet. Thus, the WT of $x(t)$ is given by

$$W(a,b)=\sqrt{a}\sum_{j=1}^{N}A_j e^{-\zeta_j\omega_{nj}t}e^{-\left(a\sqrt{1-\zeta_j^2}\,\omega_{nj}-\omega_\psi\right)^2}e^{i\sqrt{1-\zeta_j^2}\,\omega_{nj}b} \tag{2}$$

where a is the dilation parameter, which is related strictly to frequency, b represents the time parameter, ω_ψ is the wavelet frequency. For a fixed value of the dilation parameter, a=a_j, the mode whose frequency stratified equation (3) gives a relevant contribution in equation (2).

$$\omega_{nj}=\frac{\omega_\psi}{a\sqrt{1-\zeta_j^2}} \tag{3}$$

Accordingly, equation (2) can be written as

$$W(a_j,b)=\sqrt{a_j}\sum_{j=1}^{N}A_j e^{-\zeta_j\omega_{nj}t}e^{i\sqrt{1-\zeta_j^2}\,\omega_{nj}b} \tag{4}$$

Based on the wavelet property, the structural frequencies can be identified. In addition, the damping ratio can be estimated by plotting the envelope for corresponding a_j in the semi-logarithmic scale. More detailed information regarding the natural frequencies and damping identification using structural response induced by white noises is available in Ruzzene *et al.* [35] and Staszewski [36]. Table 4 summarises the fundamental frequency and damping ratio of the soil surface, raft, structure-middle and structure-top using the above methods. The fundamental principle of isolation is to elongate the fundamental period of the structure and to decrease the structural seismic response. As shown in Table 4, the fundamental frequency at the top of the structure (structure top) in case B is 7.61 Hz, which is lower than the two other cases (case A: 9.23 Hz, case B: 10.24 Hz). The fundamental period of the structure of case B is elongated by 21.29% and 34.56%, compared with case A and case C. The same trend also appears in other locations such as the soil surface, the raft, and the structure-middle. This means that the isolation efficiency of cushion B is better than cushion A and cushion C. In addition, comparing the structural frequency in case A with that in case C, the isolation efficiency of cushion A is better than cushion C.

Table 4 The fundamental frequencies and damping ratios of different cases.

Case	Soil surface		Raft		Structure-middle		Structure-top	
	f_n (Hz)	ζ (%)	f_n (Hz)	ζ (%)	f_n (Hz)	ζ (%)	f_n (Hz)	ζ (%)
Case A	9.22	3.00	9.15	3.70	9.22	3.57	9.23	3.09
Case B	7.63	3.85	9.08	3.15	7.54	4.32	7.61	3.07
Case C	8.91	4.82	8.70	3.87	9.88	5.29	10.24	3.41

3.2 Soil nonlinearity

This section investigates the seismic response of the near-pile and far-field soil and the influence of peak ground acceleration on the soil surface response. The accelerometers A4 and A5 were embedded into the soils to measure the acceleration of the soil between piles. The soil among piles is named "near-pile". Also, accelerometers A6 to A9 were embedded into the soils far away from the piles, and the soil far away from the pile is named "far-field".

The peak accelerations along soil depths in case B are shown in Figure 5, and the structural response is produced by the YG, EL, and MEX excitations with different intensities. The accelerations of the near-pile soil recorded at the depth of -0.3 m and 0.0 m are lower than the accelerations of far-field soils, and the phenomenon is similar to the results in Durante *et al.* [37] and Wang *et al.* [38]. In addition, the phenomenon would be more evident with the increase of excitation intensity because the soil-pile interaction effect is significant at the surface of the soil. The seismic response of far-field and near pile soils at the bottom of the soils is neglectable [38]. Herein, the accelerations recorded at the upper part of the soil (-0.3 m and 0.0 m) are used to investigate the difference between far-field and near-pile soils. Moreover, the acceleration amplification ratio at the soil surface under the MEX excitation is higher than the amplification ratio under the YG and EL excitations because of the resonance effect of the soil. The phenomenon is reasonable because the dominant periods of the MEX, as shown in Figure 4(d), are 0.08 s and 0.23 s, which are close to the soil fundamental period. Based on the soil surface fundamental frequency, as illustrated in Table 4, the soil fundamental period is about 0.1 s, which is range among the dominant period of MEX input motion and close to the first dominant period, 0.08 s. This is the reason why the resonance happened.

The spectrum ratio was utilised to illustrate the difference between the seismic response of the near-pile and far-field soils. The spectrum ratio was calculated as the ratio of the response spectrum of the near-surface soil at target locations (accelerometers A4, A5, A6, or A7) to that of the bottom soil (accelerometer A9) with damping of 5%. The spectrum ratios of the near-piles and the far-field soils for case B under 0.3 g and 0.6 g excitation of three ground motions are illustrated in Figure 6. The spectrum ratio of the near-pile soils is consistently slightly lower than that of the far-field soils. In addition, the spectrum ratio decreases with the increase of excitation intensity, while the dominant period increases with the increase of excitation intensity. For example, the peak spectrum ratio decreases from 3.33 to 2.89, while the dominant period increases from 0.16 s to 0.22 s. Hence, the soil nonlinearity becomes more significant with the increase of excitation intensity, which is in accordance with the results in Liang *et al.* [39]. As soil enters the plastic state as excitation intensity increases, more vibration energy is dissipated by the hysteretic soil behaviour, weakening the seismic response and extending the period. Moreover, comparing the spectrum ratio of the soil surface (Figure 6(b)) with that of the depth of -0.3m (Figure 6(a)), the former is larger than the latter. This result means the seismic response at the soil surface is more significant than the response at a depth of -0.3m.

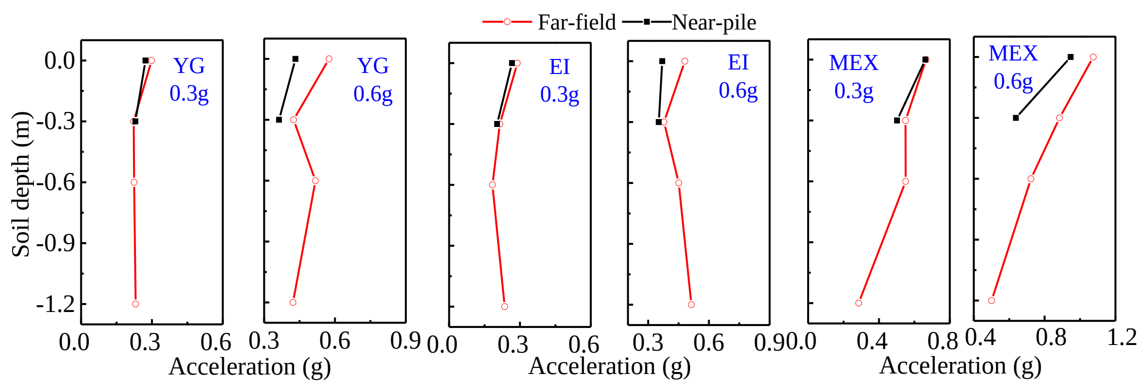

Figure 5 Peak soil acceleration along depth for far-field and near-pile soils (case B).

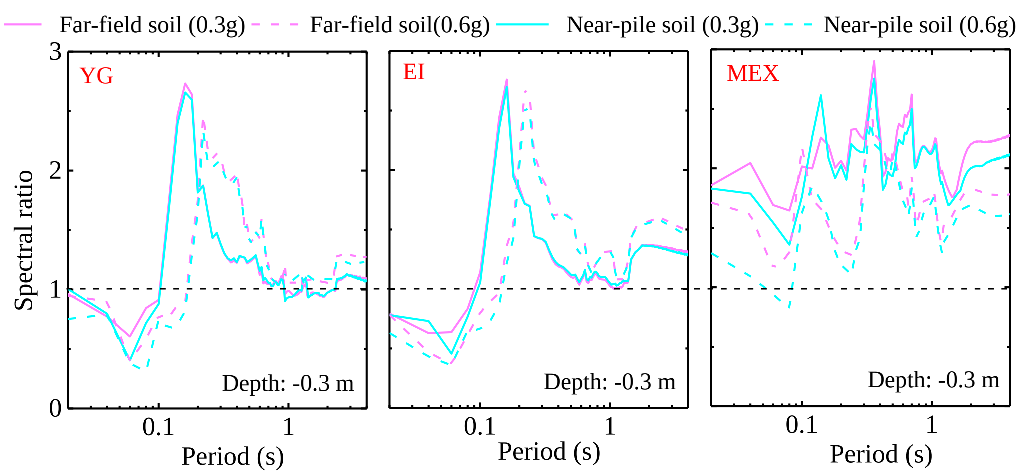

(a)

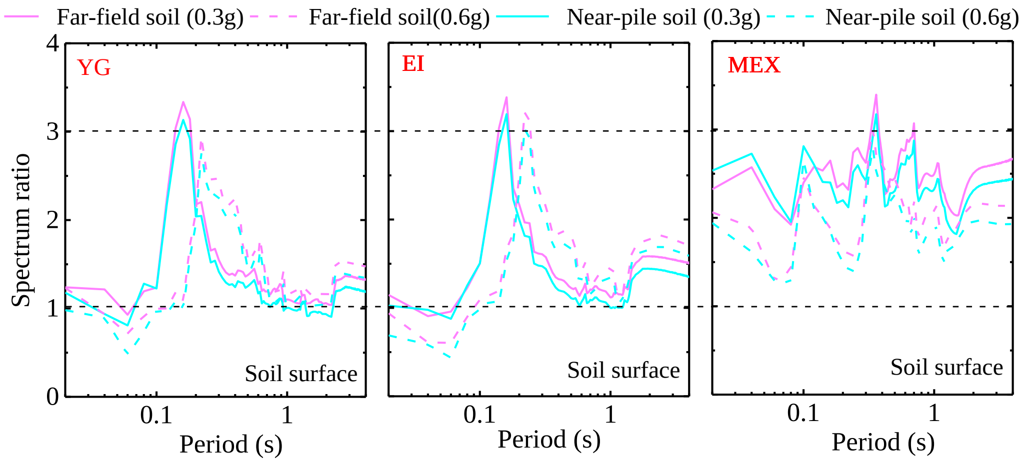

(b)

Figure 6 The spectrum ratio of near-pile and far-field pile soils for case B: (a) soils at the depth of -0.3 m; (b) soil surface.

To identify the influence of peak ground acceleration and cushion type on the seismic response of soil surface, the relationship between peak ground acceleration and soil surface acceleration of three different cases under the EL excitations is summarised in Figure 7. The peak ground acceleration is calculated using the data recorded by accelerometer A9, and the data measured by accelerometer A4 represents the acceleration at the soil surface. The acceleration at the soil surface increases with the increase of peak ground acceleration. In addition, the scatters above the dashed line in Figure 7 mean that the soil surface acceleration is higher than the peak ground acceleration under small excitation intensity. In contrast, the reverse is generally observed under higher excitation intensity. Note that the same phenomenon was also observed from the seismic response produced by the YG and MEX excitations. The soil surface acceleration results showed that the cushion type has little influence on the soil surface response.

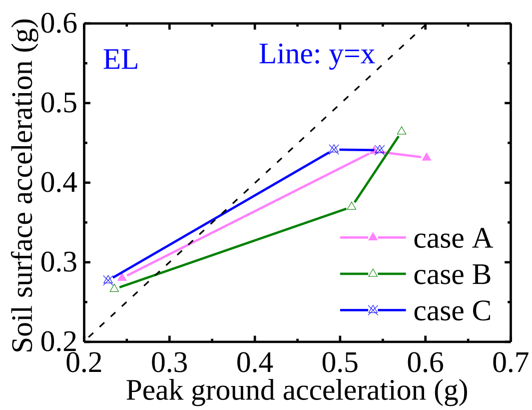

Figure 7 The influence of peak ground acceleration on the soil surface response.

3.3 Influence of cushion type on isolation effect

The accelerations of the peak ground, soil surface, and raft were utilised to study the isolation effect of different cushion types. The relationships between the peak accelerations of soil surface and raft are shown in Figure 8. Herein the data recorded at A3 and A4 represent the acceleration of the raft and soil surface, respectively. Note that two scatters, circled by the dashed line, are shown in Figure 8. They belong to the MEX data set, which may be induced by the resonance effect between the long-period ground motion and the soil. The peak acceleration of the raft increases slightly before the peak acceleration of the soil surface reaches 0.6g. However, it is likely to fluctuate at a similar level after the peak soil surface acceleration over 0.6 g, so under greater excitations, low forces and accelerations place on the superstructure, and the seismic isolation effect of gravel cushions performs well. Moreover, the peak raft accelerations in case C are generally larger than the peak soil surface accelerations in case A and case B under the same earthquake intensity excitation. This means that the base shear of case C under excitation is bigger than that of case A and case B. Hence, cushion C has a less efficient isolation effect than cushion A and cushion B.

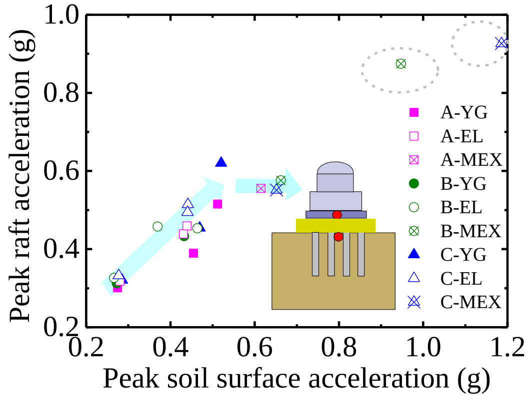

Figure 8 Relationship between the peak soil surface and raft acceleration

Figure 9 plots the influence of cushion type on the peak raft acceleration of the three cases under various earthquake excitations, considering the soil-pile-cushion-raft-structure interaction. The peak ground acceleration and peak raft acceleration are based on the accelerometers of A9 and A3, respectively. The data in Figure 9 shows that the peak raft acceleration is proportional to the peak ground acceleration under small earthquake excitation, which means the system remains in an elastic state. With the increase of peak ground acceleration, it shows a fluctuation at a similar level because the soil nonlinearity is becoming stronger and the soil-pile-cushion-raft-structure interaction. Furthermore, in general, the peak raft acceleration of case C is higher than that of the other two cases, which also implies that cushions A and B have better isolation efficiency than cushion C. This may be because there is only one kind of particle, with particle diameter ranging from 2 mm to 5 mm, for cushion C leading to the weak interparticle slip ability.

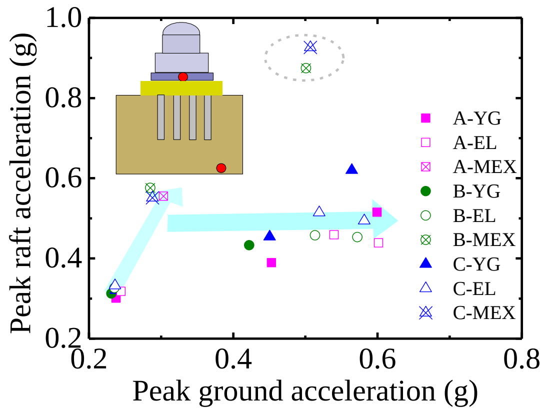

Figure 9 Relationship between peak ground and raft acceleration

4 Displacement results

4.1 Influence of peak ground acceleration on the vertical displacement

In this paper, laser displacement meters LS1 and LS2 were equipped to monitor the vertical displacements of the model under earthquake excitation. Figure 10 illustrates the vertical displacements of the structure under the YG excitation with different intensities. The vertical displacements recorded by the laser displacement meters, LS1 and LS2, were different, which means the structure generates rocking during the excitation. The vertical displacement differences for all cases under each excitation were calculated and plotted in Figure 11. Note that three test results, AM2, AM23, and BY3, are not included in Figure 11 because the displacement meter may be faulty during those tests. The absolute difference in vertical displacement under earthquake excitation is ±1.5 mm.

Figure 12 shows the settlement-rotation behaviour of the foundation under different intensity earthquake excitations. Small amounts of settlement and rocking were detected during the 0.3g YG earthquake. With the earthquake intensity increasing, the settlement and rotation angle increase. The model is asymmetric in the direction perpendicular to the shaking direction, as shown in Figure 3(a), that is the reason why the model rotated clockwisely under 0.6 g and 0.9 g earthquake excitations. The model has an inclination in the LS2 sensor direction. The distance between the laser displacement meter to the edge of the structure is about 30 mm, so the distance between two meters is equal to 382 mm, and the rotation angle when the difference in vertical displacement reaches ±1.5 mm is 1/254 (0.4%). Note that this value is obtained under the peak ground excitation nearly 0.6 g. Allmond and Kutter [40] proposed a shear key connection and found that the DPRF with a shear key has a significant improvement over the performance of the unkeyed DPRF. Xu and Fatahi [20] recently recommended that applying geosynthetic-reinforced cushioned piles could help control rocking for a pile raft foundation. Due to the high safety requirement of the nuclear power station, the rocking under earthquake excitation should be paid more attention to and more research to improve the performance of the foundation is needed when adopting a DPRF.

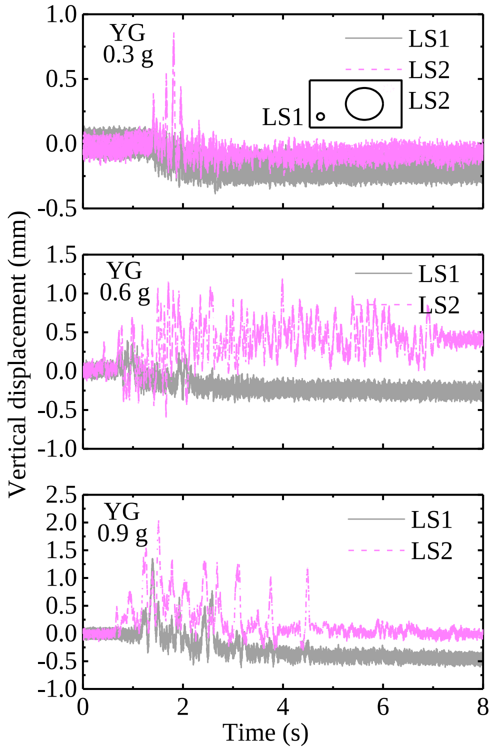

Figure 10 Vertical displacement of case C under YG excitations.

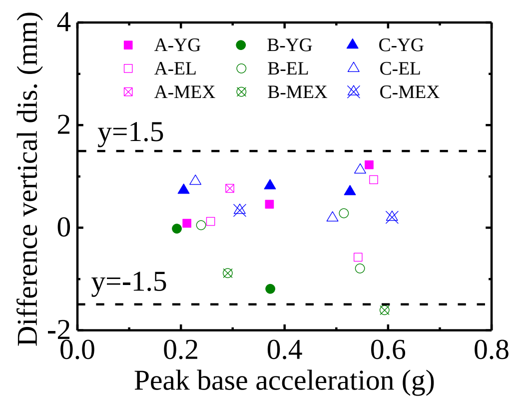

Figure 11 Influence of peak ground acceleration on difference vertical displacement.

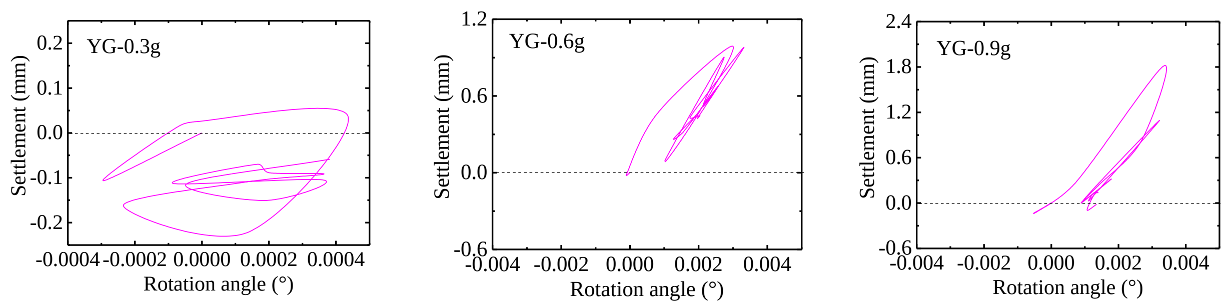

(a) under 0.3 g excitation **(b) under 0.3 g excitation** **(c) under 0.9 g excitation**

Figure 12 Settlement-rotation behavior of case C

4.2 Influence of peak ground acceleration on the horizontal displacement

The horizontal displacement is analysed based on the recorded displacement at sensors LS3 and LS4. Both LS3 and LS4 are equipped on a shelf located on the ground, so the recorded displacement by LS3 and LS4 are displacement results with respect to an observer on the ground, and the difference between LS3 and LS4 is the absolute horizontal displacement of the structure. Note that LS4 is not plotted in Figure 3, which is located at the surface of the laminar shear model box to monitor the displacement of the box. The horizontal displacement of the structure and box are illustrated in Figure 13. Under the YG excitation, with the increase of intensity, the maximum horizontal displacement is enlarged. To better understand the effect of cushion type on the horizontal displacement, the recorded data of LS3 and LS4 are utilised to calculate the absolute horizontal displacement values. Figure 14 plotted the comparison results of case A, case B, and case C. For example, under a similar 0.3 g YG excitation, the horizontal displacement of case C is lower than that for case A and case B, which means the energy dissipation ability of the cushion is smaller than the other cases.

This finding is in line with the mentioned test result of the isolation efficiency of cushion C. Also, under the MEX excitation, the difference in horizontal displacement is larger than that under the YG excitation. This may be because the MEX ground motion has a long period, resulting in a resonance during excitation.

5 Bending moment results and discussion

The bending moment is calculated utilising the recorded time history strain data obtained from the strain gauges. As described before, each instructed pile was equipped with spaced strain gauges at the depth of -0.55 m, -0.45 m, -0.35 m, -0.25 m, -0.15 m, and -0.05 m at the left and right sides of the pile. Note that the ±0 m is in line with the pile head. The peak bending moment of the pile at each strain gauge is computed using the following equation.

$$M = \frac{EI(\varepsilon_t - \varepsilon_c)}{2r} \tag{5}$$

where E is the elasticity modulus of the pile; I is the inertia moment of the pipe pile; ε_t is the average tension strain of Max left (ε_{t1}) and Max right (ε_{t2}); ε_c is the average compression strain of Min left (ε_{c1}) and Min right (ε_{c2}); r is the radius of the pile. The strain data of left and right have opposite signs, which means when one side is tension side, the other side is compression side. For instance, ε_{t1} and ε_{c1} happen almost simultaneously due to the time lag between data acquisition channels. The piles in tests are symmetric tube piles, and the maximum bending moment can be generated by $EI(\varepsilon_{t1} - \varepsilon_{c1})/2r$ or $EI(\varepsilon_{t2} - \varepsilon_{c2})/2r$, therefore, the average of those values, as shown in equation (5), was utilised in this paper. Besides, the relationship between strain and bending moment of piles was calibrated based on the cantilever beam theory, and the results showed excellent agreement. Please note that the magnitudes of bending moment are of model scale and for the comparative purpose only, and so are not able to compare with practical design value.

5.1 Influence of peak ground acceleration and earthquake

Figure 15 shows the pile bending moment of P-1 for the three cushion cases under different EL excitation scenarios. The test results show similar bending moments for case A, case B, and case C, which means the cushion type has little effect on the bending moment of the pile for DPRF. Therefore, only the results of case A is illustrated in this part.

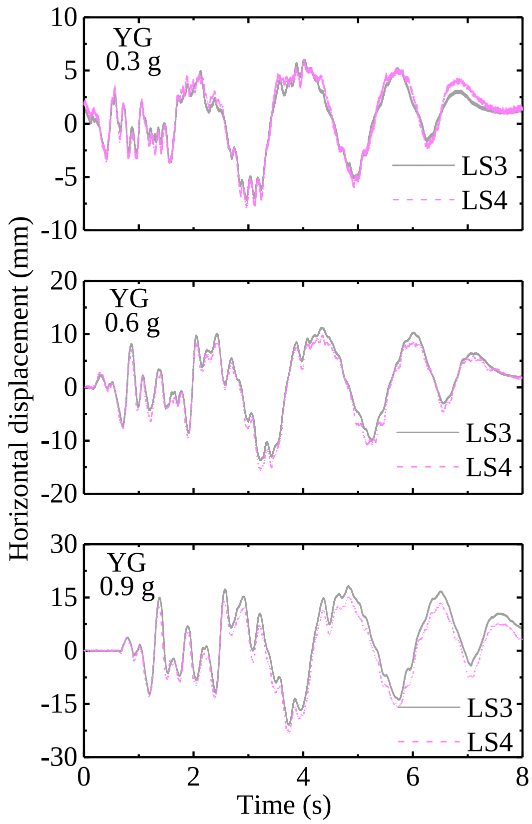

Figure 13 Horizontal displacement of case C under YG excitations.

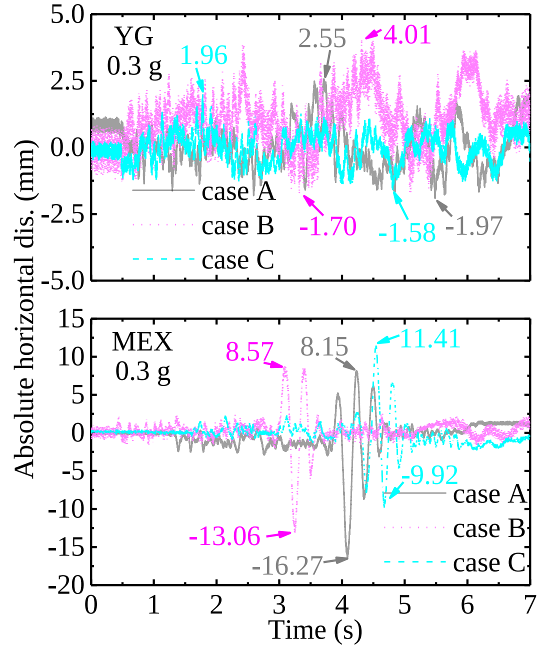

Figure 14 Influence of cushion type on the absolute horizontal displacement.

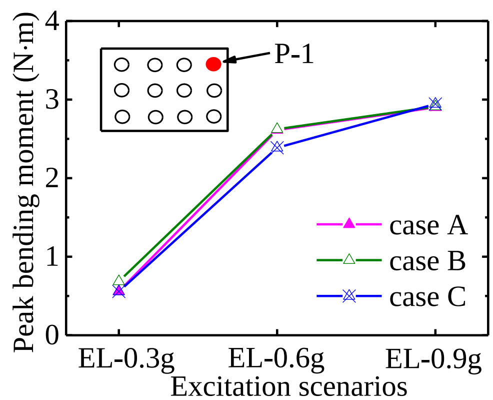

Figure 15 Piles bending moment of P-1 for different cases under EL excitations.

Figure 16 plots the peak bending moment of four instructed piles for case A under different earthquake excitations. In general, the graph shows a gradual increase in the value of peak bending moment of piles with increased excitation intensity. For example, the peak bending moment of P-1 at the depth of -0.35 m under excitation of three intensity YG excitation are 1.04, 3.79, and 4.76 N·m, respectively. Moreover, this phenomenon is the same under the EL and MEX excitation because the higher intensity excitation effect is more significant on the seismic system response. Figure 16 (a), (b), and (c) generate the bending moment of piles under the excitation of YG, EL, and MEX. The test results under YG and EL excitation are close to each other; however, it shows a significant increase under the MEX excitation. For illustration, the peak bending moment of P-1 at the depth of -0.35 m under 0.9 g earthquake excitation are 4.76, 4.27, and 11.11 N·m, respectively. The most likely reason is that the MEX is a long-period ground motion, which may cause a resonance effect during excitation.

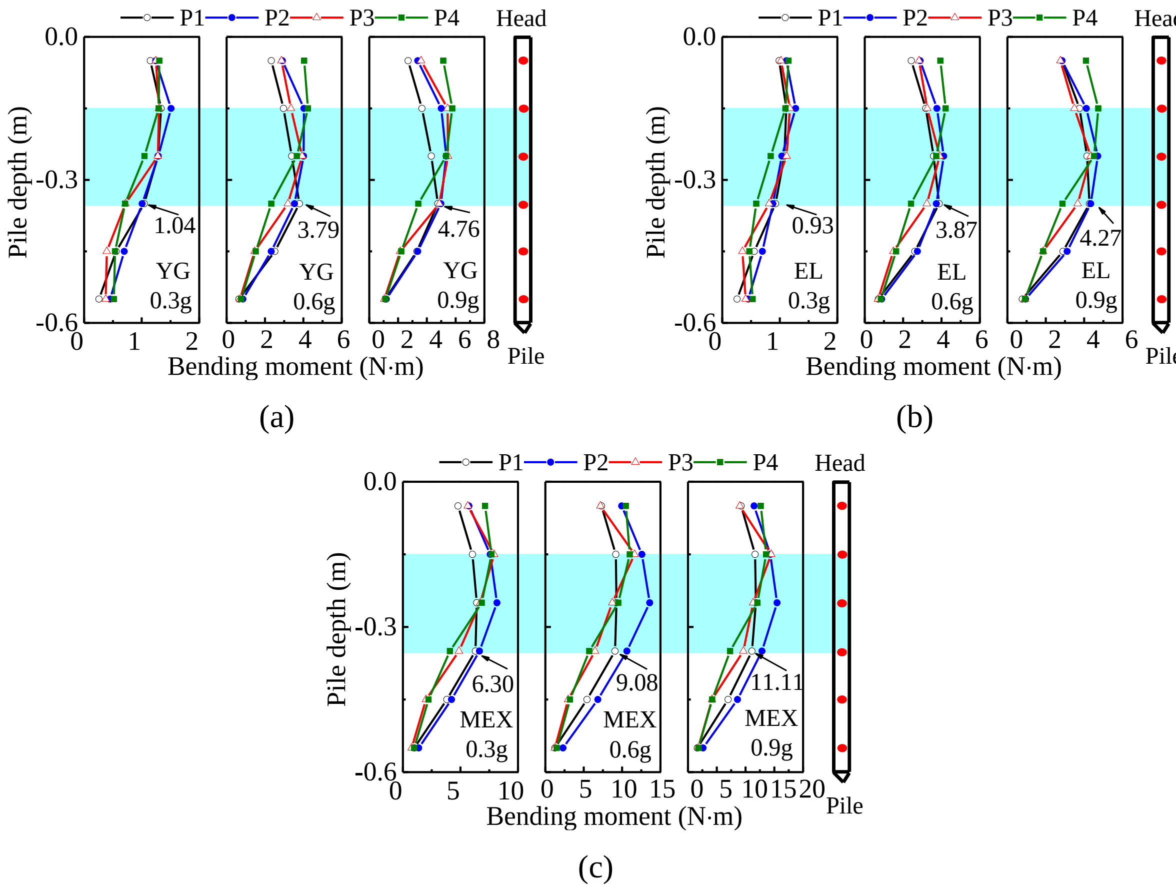

Figure 16 Instructed piles bending moment for case A: (a) pile bending moment of case A under YG excitation; (b) pile bending moment of case A under EL excitation; (c) pile bending moment of case A under MEX excitation.

In terms of the location of the maximum bending moment along with piles, the bending moment at the middle of depths of the pile is large, as shown in the shadow zone in Figure 16 from the depth of -0.35~-0.15 m. Comparing the maximum bending moment along with piles of P-1, P-2, P-3, and P-4, it turns out that the maximum bending moment of piles is irrelevant to the location of the pile, which means the pile-to-pile interaction may have a slight effect on the bending moment for DPRF. The disconnection of pile raft is the main effect on this characteristic of pile bending moment. This research result is consistent with the finding of Ko *et al.*[22]. More in-depth details about the peak bending moment at different depths will be explained in the following part.

5.2 Characteristics of peak bending moment

Figure 17 shows the relationship between peak near-pile soil acceleration and the peak bending moment of the piles at the depth of -0.45 m for all cases. The peak near-pile soil acceleration is the acceleration recorded by the accelerometer A5, which is located at the depth of -0.3 m, close to the strain measuring point at the depth of -0.45 m. The strain measuring point is outside the shadow zone, among which the bending moment of the pile is larger than the other areas. A significant focus on the relationship between those two parameters could produce interesting findings that the peak bending moment of instructed four piles at the depth of -0.45 m is proportional to the peak near-pile soil acceleration. In addition, the slope for the edge pile (P-1 and P-3) is higher than that of P-2 and P-4. In order to make a comparison between the bending moment at different depths, the peak bending moment of piles at the depth of -0.25 m is summarised in Figure 18. It is noted that the measuring point at the depth of -0.25 m is among the maximum bending moment area (light blue zone of the figures). The relationship between the peak near-pile soil accelerations and peak bending moments also shows the same linear feature. However, there is a slight difference from various locations, which is already illustrated above. In general, closer to the bottom of the pile, the bending moment shows a stronger dependence on the location of the pile than that at the middle area of the piles where maximum bending moment occurs.

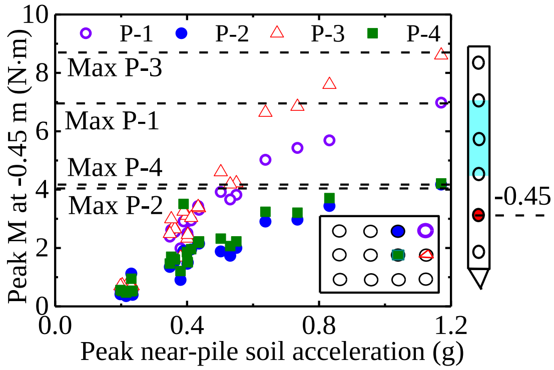

Figure 17 Peaking bending moment of piles at the depth of -0.45 m.

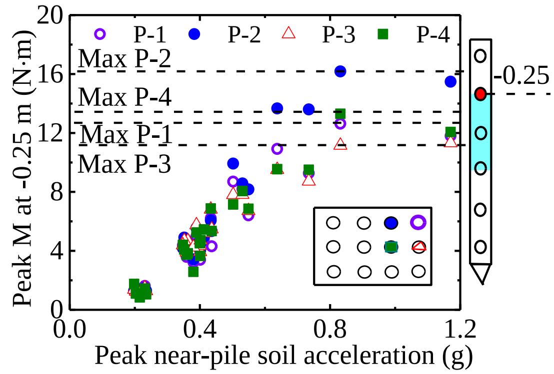

Figure 18 Peaking bending moment of pile at the depth of -0.25 m.

Conclusions

A series of 1 g shaking table tests on a scaled nuclear power station were carried out to study the seismic response of the structure with DPRF using three types of cushions. A well-graded gravel (cushion A), a gap-graded mixture of two gravels (cushion B), and a single small size gravel (cushion C) were adopted in the tests to investigate the influence of cushion type. The following main conclusions were drawn from this study:

1. The fundamental frequency obtained based on the white noise excitation showed that cushion B and cushion A with a wider particle size range had better isolation efficiency than case C. And the absolute horizontal displacements for case C is the smallest among all cases, which means the earthquake energy dissipation ability for case C is lower than the other cases. Accordingly, the granular composition is an important influence factor for the isolation effect of the structure with the DPRF.
2. The near-pile acceleration and the spectrum ratio at the top of the near-field soil were lower than that of the far-field soils. This phenomenon was more significant with the increase of earthquake intensity. Moreover, the acceleration increase ratio at the soil surface under short-period excitation was higher than that under the long-period excitation.
3. Comparing the peak accelerations of the raft of difference cases, case C was generally the biggest. This result also implied that cushion C was less efficient in isolation. For all DPRF cases, the peak acceleration of the raft showed a linear relationship between the peak soil surface acceleration and the peak ground acceleration under small excitation intensity. However, at high excitation intensity, the peak acceleration shows a fluctuation at a similar level.
4. The maximum bending moment was found to appear in the middle of the piles, and the maximum bending moment of piles was irrelevant to the location of piles. An interesting finding was that the peak bending moment of instrumented piles at the depth of -0.45 m, out of the maximum bending moment area, was proportional to the peak near-pile acceleration. The cushion type used in the tests had slight influences on the bending moment of piles.

Considering the benefits of the isolation effect, the DPRF is recommended for nuclear power stations rested in clay, but studies on nuclear power stations rested in clay with DPRF are not enough. The granular composition of the cushion layer is an important impactor on the isolation effect, and based on the tests in this paper, well-graded and gap-graded gravels perform better than the single small size gravel. However, there are some limitations of this study. The cushion material may contain rubber or geosynthetic materials, and this study only compared three different gravel cushions and more research for isolation cushions is needed. More effort should be put into exploring measures to control the movement of the superstructure with DPRF. Moreover, the punching issue was not measured in the tests. In addition, the comparison between CPRF and DPRF cases will be analysed in future studies.

Acknowledgements

The authors would like to gratefully acknowledge the supports from the Scientific Research Program of China General Nuclear Power Corporation (CGN) (Grant No. K-A2017.054), Postgraduate Research and Practice Innovation Program of Jiangsu Province (Grant No. KYCX19_0093), and the National Construction of High-level University Public Graduate Project (Grant No. CSC201906090102).

References

[1] Davis EH, Poulos HG. The analysis of piled raft systems. *Australia Geotechnique Journal* 1972; 2:21-27.
[2] Poulos HG. Piled raft foundations: design and applications. *Geotechnique* 2001; 51(2): 95-113.
[3] Cooke RW. Piled raft foundations on stiff clays-a contribution to design philosophy. *Geotechnique* 1986; 36(2): 169-203.
[4] Chow YK, Thevendran V. Optimisation of pile groups. *Computers and Geotechnics* 1987; 4(1): 43-58.
[5] Randolph MF. Design methods for pile groups and piled rafts. *Proceeding 13th International Conference on Soil Mechanics and Foundation Engineering*, New Delhi 1994; 2:61–82.
[6] Kim KN, Lee SH, Kim KS, Chung CK, Kim MM, Lee HS. Optimal pile arrangement for minimising differential settlements in piled raft foundations. *Computers and Geotechnics* 2001; 28(4): 235-253.
[7] Pecker A. Enhanced seismic design of shallow foundations: example of the Rion Antirion bridge. *In Proceedings of the 4th Athenian Lecture on Geotechnical Engineering*, Hellenic Society of Soil Mechanics and Geotech- nical Engineering, Athens 2006. 1–23.
[8] Mattsson N, Menoret A, Simon C, Ray M. Case study of a full-scale load test of a piled raft with an interposed layer for a nuclear storage facility. *Géotechnique* 2013; 63(11): 965-976.
[9] Liang FY, Li TD, Qian Y, Wang C, Jia YJ. Investigating the seismic isolation effect of the cushioned pile raft foundation in soft clay through dynamic centrifuge tests. *Soil Dynamics and Earthquake Engineering* 2021; 142: 106554.
[10] Wong IH, Chang MF, Cao XD. Raft foundations with disconnected settlement reducing piles. *In design application of raft foundations and ground slabs*. London: Thomas Telford; 2000. 469-486.
[11] Liang FY, Chen LZ, Shi XG. Numerical analysis of composite piled raft with cushion subjected to vertical load. *Computers and Geotechnics* 2003; 30(6): 443-453.
[12] Ata A, Badrawi E, Nabil M. Numerical analysis of unconnected piled raft with cushion. *Ain Shams Engineering Journal* 2015; 6(2): 421-428.
[13] El Sawwaf M. Experimental study of eccentrically loaded raft with connected and unconnected short piles. *Journal of Geotechnical and Geoenvironmental Engineering* 2010; 136(10): 1394-1402.
[14] Tradigo F, Pisanò F, Di Prisco C. On the use of embedded pile elements for the numerical analysis of disconnected piled rafts. *Computers and Geotechnics* 2016; 72: 89-99.
[15] Tradigo F, Pisanò F, Di Prisco C, Mussi A. Non-linear soil–structure interaction in disconnected piled raft foundations. *Computers and Geotechnics* 2015; 63: 121-134.
[16] El Kamash W, El Naggar H, Nabil M, Ata A. Optimising the unconnected piled raft foundation for soft clay soils: numerical study. *KSCE Journal of Civil Engineering* 2020; 1-8.
[17] Dutta SC. Saha R, Haldar S. Inelastic seismic behavior of soil–pile raft–structure system under bi-directional ground motion. *Soil Dynamics and Earthquake Engineering* 2014; 67: 133-157.
[18] American Society of Civil Engineers (ASCE). Minimum design loads for buildings and structures. 2005. SEI 7-05.
[19] CEN E. Design of structures for earthquake resistance, Part-1: General rules, seismic actions and rules for buildings. European Committee for Standardization. 2004.
[20] Xu R, Fatahi B. Geosynthetic-reinforced cushioned piles with controlled rocking for seismic safeguarding. *Geosynthetics International* 2018;25:561–81.
[21] Azizkandi AS, Baziar MH, Yeznabad AF. 3D dynamic finite element analyses and 1 g shaking table tests on seismic performance of connected and nonconnected piled raft foundations. *KSCE Journal of Civil Engineering* 2018; 22(5): 1750-1762.
[22] Baziar MH, Rafiee F, Lee CJ, Saeedi Azizkandi A. Effect of superstructure on the dynamic response of nonconnected piled raft foundation using centrifuge modeling. *International Journal of Geomechanics* 2018; 18(10): 04018126.

[23] Ko KW, Park HJ, Ha JG, Jin S, Song YH, Song MJ, Kim DS. Evaluation of dynamic bending moment of disconnected piled raft via centrifuge tests. *Canadian Geotechnical Journal* 2019; 56(12): 1917-1928.
[24] Saadatinezhad M, Lakirouhani A, Jabini Asli S. Seismic response of non-connected piled raft foundations. *International Journal of Geotechnical Engineering* 2019; 1-15.
[25] Ha JG, Ko KW, Jo SB, Park HJ, Kim DS. Investigation of seismic performances of unconnected pile foundations using dynamic centrifuge tests. *Bulletin of Earthquake Engineering* 2019; 17(5): 2433-2458.
[26] Dhanya JS, Boominathan A, Banerjee S. Response of low-rise building with geotechnical seismic isolation system. *Soil Dynamics and Earthquake Engineering* 2020;136:106187.
[27] Yang Y, Gong W, Cheng YP, Dai G, Zou Y, Liang F. Effect of soil-pile-structure interaction on seismic behaviour of nuclear power station via shaking table tests. Structures 2021;33:2990–3001. https://doi.org/10.1016/j.istruc.2021.06.051.
[28] Zeng LL, Hong ZS, Cai YQ, Han J. Change of hydraulic conductivity during compression of undisturbed and remolded clays. *Applied Clay Science* 2011; 51(1-2): 86-93.
[29] Tu WB, Huang MS, Gu XQ. Dynamic behavior of laterally loaded caisson foundations based on different cushion types: an experimental and theoretical study. *Journal of Zhejiang University-SCIENCE A* 2020; 21(7): 565-579.
[30] Lu XL, Zhou Y, Lu WS. Shaking table model test and numerical analysis of a complex high-rise building. *The Structural Design of Tall and Special Buildings* 2007; 16(2): 131-164.
[31] Liu H, Mi XW, Li YF, Duan Z, Xu YN. Smart wind speed deep learning based multi-step forecasting model using singular spectrum analysis, convolutional Gated Recurrent Unit network and Support Vector Regression. *Renewable Energy* 2019; 143: 842-854.
[32] Ma XJ, Jin Y, Dong QL. A generalised dynamic fuzzy neural network based on singular spectrum analysis optimised by brain storm optimisation for short-term wind speed forecasting. *Applied Soft Computing* 2017; 54: 296-312.
[33] Niu T, Wang JZ, Zhang KQ, Du P. Multi-step-ahead wind speed forecasting based on optimal feature selection and a modified bat algorithm with the cognition strategy. *Renewable Energy* 2018; 118: 213-229.
[34] Wen Q, Hua XG, Chen ZQ, Niu HW, Wang XY. AMD-based random decrement technique for modal identification of structures with close modes. *Journal of Aerospace Engineering* 2018; 31(5): 04018057.
[35] Ruzzene M, Fasana A, Garibaldi L, Piombo B. Natural frequencies and dampings identification using wavelet transform: application to real data. *Mechanical Systems and Signal Processing* 1997; 11(2): 207-218.
[36] Staszewski WJ. Analysis of non-linear systems using wavelets. *Proceedings of the Institution of Mechanical Engineers, Part C: Journal of Mechanical Engineering Science* 2000; 214(11): 1339-1353.
[37] Durante MG, Di Sarno L, Mylonakis G, Taylor CA, Simonelli AL. Soil-pile-structure interaction: experimental outcomes from shaking table tests. *Earthquake Engineering and Structural Dynamics* 2016; 45(7): 1041-1061.
[38] Wang XW, Ye AJ, Shang Y, Zhou LX. Shake-table investigation of scoured RC pile-group-supported bridges in liquefiable and nonliquefiable soils. *Earthquake Engineering and Structural Dynamics* 2019; 48(11): 1217-1237.
[39] Liang FY, Liang X, Zhang H, Wang C. Seismic response from centrifuge model tests of a scoured bridge with a pile-group foundation. *Journal of Bridge Engineering* 2020; 25(8): 04020054.
[40] Allmond JD, Kutter BL. Design considerations for rocking foundations on unattached piles. *Journal of Geotechnical and Geoenvironmental Engineering* 2014; 140(10): 04014058.